Journal of Materials Chemistry C

Accepted Manuscript

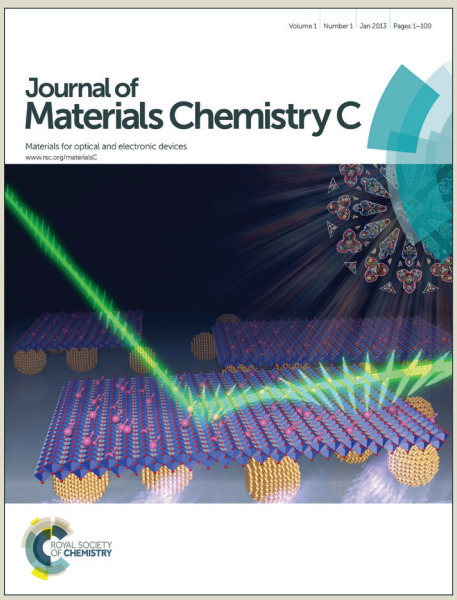

ROYAL SOCIETY OF CHEMISTRY

www.rsc.org/materialsC

Room temperature ferromagnetism in SnO_2 nanoparticles: An experimental and Density Functional study

Pawan Chetri, Biswajit Choudhury* and Amarjyoti Choudhury

Department of Physics, Tezpur University, Napaam, Tezpur-784028, India.

Abstract

Room temperature ferromagnetism is observed in pristine SnO_2 nanoparticles prepared via sol-gel method. Microstructural studies with XRD and Raman reveal the coexisting of SnO and SnO_2 phase in vacuum annealed SnO_2. Electron paramagnetic resonance (EPR) results confirm the presence of paramagnetic trapped hole in lattice oxygen atom and superoxide radical species in air and vacuum annealed SnO_2 respectively. It is seen that growth condition has significant influence on the magnetism of the nanoparticle. Air and vacuum annealed SnO_2 display clear ferromagnetic behavior at room temperature. However, the saturation magnetization reduces in vacuum annealed SnO_2. We have compared the experimental results with ab initio density functional calculations and observed that the Sn vacancies are the main reason of magnetism in SnO_2. The pattern of theoretical formation energy values shows that it is easier to form Sn vacancies in SnO_2 under O rich limit (similar to air annealing). This is in conformity with the experimentally determined higher saturation magnetization values in air annealed SnO_2. Spin polarization of lattice oxygen atom by the presence of Sn vacancy gives rise to magnetism.

Keywords: Room temperature ferromagnetism, SnO_2, DFT calculations, Oxygen vacancies.

For correspondence: *Email: biswajit@tezu.ernet.in, Phone: +919401313177.

1. Introduction

In the field of spintronics it is important to design semiconductors with ferromagnetically polarized carriers at room temperature (RT).[1] The understanding of spin-based devices for quantum information depends upon the improvement of various nanoscale semiconductor architectures that allows perfect isolation and coherent control of the quantum confined spin states.[2] Room temperature ferromagnetism in transition metal doped semiconductor oxides is widely reported.[2-5] However, the formation of extrinsic magnetic impurity clusters stand as an obstacle in the practical applications of these materials. Hence, the quest is for RT ferromagnetism in a semiconductor material with appreciable saturation magnetization. Undoped oxide materials seem to be a better candidate for spintronics as the possibility of extrinsic magnetic phase separation due to magnetic impurities could be avoided. There are reports of ferromagnetism in undoped SnO_2 nanosystems.[6- 8] Few authors[7-10] have claimed that the observed ferromagnetism in pristine SnO_2 is due to the presence of oxygen vacancies. On the other hand authors[11,12] have claimed on theoretical grounds that the main reason behind the observed ferromagnetism in the SnO_2 system is the presence of Sn^{4+} vacancy. Espinosa et.al[12] confirmed that Sn^{4+} vacancies are the main source of magnetism in SnO_2 thin film. Similarly, Rusydi *et al.*[13] and Qi *et al.*[14] justified with experimental and theoretical approach cationic (Ti) vacancy mediated ferromagnetism in Ta doped TiO_2. Ghosh *et al*., however, reported diamagnetism in pure SnO_2 nanoparticles.[15] Therefore, the exact origin of ferromagnetism in these nanoparticles is not clearly explained.

In this article we have performed both experimental and theoretical studies to establish the dependence of growth condition (oxygen rich or oxygen deficient) on the magnetism of SnO_2 nanoparticles. Initial characterization results of XRD and Raman show the coexisting of SnO and SnO_2 phases in vacuum annealed SnO2. We have used density functional (DFT) calculation using MedeA VASP (Vienna ab-initio simulation package) 5.2 for the investigation of intrinsic cause of magnetism in pristine SnO_2 prepared under both air and vacuum condition. Finally, we have verified on experimental

and theoretical ground the influence of cationic Sn^{4+} vacancy and anionic oxygen vacancy on ferromagnetism in SnO_2.

2. Synthesis of SnO_2 nanoparticles: The synthesis of SnO_2 followed sol-gel procedure.[16] All the reagents were of AR grade. The reagents used were $SnCl_2.2H_2O$ (98 % Merck), double distilled water, ethanol (Merck), HCl (Merck), and ammonia solution (Merck). 1g of $SnCl_2.2H_2O$ was mixed with 11 ml double distilled water and 5 ml ethanol. The above solution was stirred for 15 minutes and then few drops of HCl was added. Ammonia solution was added drop wise till the pH = 10 were attained. The prepared gel was divided into two parts. One part was dried at 60^0C and annealed at 200^0C. The other part was dried and annealed in vacuum at 60^0C and 200^0C respectively. The sample annealed in air was named TO200, while the sample annealed in vacuum was quoted in this manuscript as $TO_{Vac}200$.

3. Experimental and computational details: X-ray diffraction pattern of the nanoparticles was monitored in a Bruker AXS D8 focus X-ray diffractometer (XRD) equipped with intense Cu Kα radiation (λ=0.154 nm). The scanning speed was 0.5 sec/step with an increment of 0.0057 degree. High resolution transmission electron microscope (HRTEM) images of the prepared nanoparticles were obtained with JEOL JEM 2010 transmission electron microscope operating at a voltage of 200 kV. Elemental analysis of the as prepared SnO_2 nanopowder was studied with inductively coupled plasma optical emission spectroscopy (ICP-OES) in Perkin Elmer Optima 2100 DV by digesting the sample completely in small volume of conc. HNO_3. Raman spectra of the samples were obtained in Renishaw in Via Raman spectrometer with an Ar^+ ion laser of 514.5 nm wavelength with spectral resolution of 0.3 cm^{-1}. X-ray photoelectron spectra (XPS) were recorded on a Kratos Axis 165 XPS spectrometer equipped with dual aluminum–magnesium anodes using Mg Kα radiation (hυ = 1253.6 eV). The dc magnetization measurement for the as-prepared sample was performed with a Quantum Design MPMS superconducting quantum interference device (SQUID) VSM Ever Cool system at room temperature (RT). The ZFC (zero field cooling) and FC (field cooling) temperature dependent magnetization (M-T) measurements were

done in the temperature range of 5-350 K. Electron paramagnetic resonance (EPR) was performed using JES - FA200 ESR Spectrometer in X band, sensitivity -7x10^9 spins/0.1mT and resolution - 2.35(micro) T or better .We performed density functional calculations using generalized gradient approximation (GGA) functional with Perdew-Burke-Ernzerhof (PBE) to describe the electron-electron exchange and correlation effects. The density functional theory (DFT) equations were solved via projector augmented wave (PAW) method using plane wave basis set as implemented in Vienna ab initio Simulation Package (VASP) and interfaced with MedeA technology platform. All the systems were calculated on a real space grid defined with a plane-wave energy cut off of 480 eV. A spacing of 0.3 ($\mathring{A}$)$^{-1}$ was used for K point sampling in both supercell and surface calculation. All atomic positions were fully relaxed until all atomic forces were smaller than 0.01 eV/$\mathring{A}$. A 2×2×2 supercell was built with the unit cell of SnO_2 in rutile form and with a 10 $\mathring{A}$ vacuum space between two supercells. The space group of pure SnO_2 was taken as $P_{42/mnm}$ and the Supercell contained 48 atoms ($Sn_{16}O_{32}$). The effect of Sn vacancy was investigated by removing Sn atom from centre position of the Supercell. Similarly process was done for O vacancy but for Sn interstitial an extra Sn was added in the above mentioned supercell ($Sn_{16}O_{32}$). In all the cases, spin polarized structural optimization was performed such that the systems obtained its minimum energy configuration by relaxing all the atoms in all direction and calculated the magnetic moments. For the surface (110) we also considered 48 atoms and relaxed the structure. A 10 $\mathring{A}$ vacuum slab was considered between two surfaces.

4. Results and discussion

4.1 Structural characterizations

X-ray diffraction patterns of the prepared SnO_2 nanoparticles were shown in Fig. 1. All the diffraction peaks were indexed to rutile (JCPDS-41-1445) phase. XRD graph indicated presence of SnO (101), (200) and (112) characteristic peaks along with SnO_2 phase in $TO_{Vac}200$, whereas these peaks are

missing in TO200. Surface oxygen vacancies are easily formed in the as prepared SnO_2 under vacuum annealing. SnO_2 tries to compensate these oxygen vacancies by transforming itself to SnO.[17] Crystallite sizes of all the prepared systems are calculated using Scherer's formula in the EVA software equipped with the XRD instrument. The determined values are 5.44 nm for TO200 and 12.5 nm for $TO_{Vac}200$. We believe that larger crystallite in $TO_{Vac}200$ is most likely due to the coexistence of SnO_2 and SnO crystalline phases. We further studied the morphology, size and shape of SnO_2 with high resolution transmission electron microscope (HRTEM). Fig. 2 (a-b) displays the HRTEM images of $TO_{Vac}200$ and TO200 respectively. These images show that particles are of varied sizes and shapes. Particles in $TO_{Vac}200$ are of larger size and lesser agglomerated than in TO200. The size distribution plot shows that the particles of sizes 13 nm and 6 nm are highly populated in $TO_{Vac}200$ and TO200 respectively. This compliments the crystallite sizes obtained from XRD.

Raman spectroscopy is an efficient tool to explore the vibrational modes within the system. The Raman spectra of both the prepared system is shown in Fig. 3. A normal mode can be described by the 3n (n is the number of atoms in the primitive cell) coordinates giving the displacements of the atoms from their equilibrium positions. Rutile SnO_2 having 6 atoms unit cell give out 18 possible vibrations. The normal lattice vibration at the Γ point of the Brillouin zone is as follows.[18,19]

$$\Gamma = \Gamma_1^+(1A_{1g}) + \Gamma_2^+(1A_{2g}) + \Gamma_3^+(1B_{1g}) + \Gamma_4^+(1B_{2g}) + \Gamma_5^-(1E_g) + \Gamma_1^-(1A_{2u}) + 2\,\Gamma_4^-(B_{1u}) + 4\Gamma_5^+(E_u) \quad (1)$$

Two modes (A_{2u} and triply degenerate E_u) are infrared active. E_u has two acoustic and one optic mode while A_{2u} has one optic and one acoustic mode. Four modes, viz., A_{1g}, B_{1g}, B_{2g} and doubly degenerate E_g are found to be Raman active and two (A_{2g}, B_{1u}) modes are silent. Raman active modes for rutile SnO_2 (bulk) are expected at 123, 476, 634 and 778 cm^{-1} for B_{1g}, E_g, A_{1g} and B_{2g} respectively.[20] In our case only A_{1g} peak is prominent in both the samples. Both samples exhibit a hump at 574 cm^{-1} which is refereed as the A_1 mode and is due to surface phonon in SnO_2 nanocrystallites.[21] One small peak is observed at 210 cm^{-1} in$TO_{Vac}200$ which is otherwise absent in TO200. This peak appears owing to the presence of small

fraction of SnO phase alongside SnO_2 phase. [22,23] The Raman active modes of SnO_2 (or SnO) are due to the polarization occurring due to the displacements of Sn and oxygen in Sn and oxygen sub-lattice in SnO_2. Any changes in the stoichiometry (by the presence of oxygen vacancies) in the basic SnO_6 unit (in SnO_2) and in SnO_4 (in SnO) may significantly reduces the polarization of Sn-O bond and thus, might influence the position, intensity of Raman modes. We have observed blue shifting in the position of the A_{1g} as well as surface A_1 phonon Raman mode in $TO_{Vac}200$ as compared to TO200. The blue shifting can be associated with presence of oxygen vacancies in the $TO_{Vac}200$. Presence of oxygen vacancies reduces the numbers of polarized Sn-O bond in $TO_{Vac}200$, resulting in the shifting in the position of Raman peak. Similar type of oxygen defect assisted blue shifting of Raman peak is reported in vacuum annealed SnO_2 as compared to its air annealed counterpart by Shek *et al*. [21]

Room temperature EPR spectra $TO_{Vac}200$ and TO200 are shown in Fig. 4. The *g* value is calculated using the relation

$$g = h\nu / \mu_B B \qquad (2)$$

Where *h* is the Planck's constant, *v* is the applied microwave frequency (9.878 GHz), μ_B is the Bohr magneton and *B* is the resonance magnetic field. TO200 contains an intense EPR signal at $g = 2.04$. This signal can be attributed to hole trapped at lattice oxygen site (O^- center).[24,25] $TO_{Vac}200$ contains a broad EPR signal at g ~ 2.17. This EPR signals resemble the *g*-value corresponding to superoxide radical.[26,27] The superoxide radicals (O_2^-) are formed by the transfer of trapped electron present in oxygen vacancies to the surface adsorbed O_2 molecule in SnO_2. These superoxide radicals are strongly attached to Sn^{4+} or Sn^{2+} species on the surface. Surfaces in $TO_{Vac}200$ containing high density of oxygen vacancies with trapped electrons are active sites for easy adsorption of O_2 molecule. Therefore, TO200 contain EPR signal due to hole trapped at oxygen lattice site, but does not contain any signal corresponding to oxygen vacancy or superoxide species. On the other hand $TO_{Vac}200$ contains EPR signal corresponding to oxygen

vacancies only but no signals of hole trapped oxygen. The relative number of spins participating in the broadening and intensity of EPR signal are calculated by the relation[28]

$$N_s \propto I\,(\Delta H)^2 \qquad (3)$$

I and (ΔH) are the intensity and FWHM of the intense peak calculated from the integrated spectrum of each sample. It is found that relative number of spins (N_s) due to electron trapped in oxygen vacancy is higher than that of hole trapped at oxygen lattice site, viz., N_s in $TO_{Vac}200 > TO200$.

We have carried out XPS analysis of $TO_{Vac}200$ (Fig. 5) and TO200 (Fig. 6). The standard $3d_{5/2}$ spectrum for Sn^{4+} and Sn^{2+} are found to be at 486.72 and 487.4 eV respectively.[29,30] The separation between Sn $3d_{5/2}$ and Sn $3d_{3/2}$ should be around 8.5 eV.[30] In TO200 the peaks found for Sn^{4+} are at 486.9 and 495.4 eV while in $TO_{Vac}200$ the peaks for Sn^{4+} are obtained at 486.7 and 495.2 eV. The peaks of Sn^{2+} in $TO_{Vac}200$ are found to be at 488.1 and 496.6 eV. We have not observed any Sn^{2+} peak in TO200 which confirms the absence of SnO in TO200. The separation between $3d_{5/2}$ and $3d_{3/2}$ spectra of Sn^{4+} and Sn^{2+} is 8.5 eV, although peaks are found to be shifted to higher energy in comparison to standard spectrum. The peaks of Sn^{2+} are found to be shifted to higher energy by 0.7 eV with respect to the standard sample value (given above). O 1s spectra of both the sample is deconvoluted into two peaks. The peak in lower energy can be ascribed to lattice oxygen (O_L) while the higher energy one is due to adsorbed oxygen at the surface (O_H). [29n31] The percentage concentration of O_L and O_H is found to be 59.5 and 40.5 respectively for TO200 while it is 53.6 and 46.4 respectively for $TO_{Vac}200$. The amount of adsorbed oxygen in $TO_{Vac}200$ increases than in TO200. Actually, in $TO_{Vac}200$ the number of oxygen vacancies increases such that the surface becomes more reactive and hence adsorb large numbers of free oxygen molecules.

4.2 Magnetic properties study

Prior to the magnetic measurements ICP-OES elemental analysis for the magnetic impurity Fe, Co and Ni are carried out. The concentration of Fe, Co and Ni is found to be 0.088, 0.003 and 0.085 ppm

respectively. The form of these impurities can be in pure metal phase or in metal oxide phase. FeO and α-Fe_2O_3 are anti ferromagnetic whereas γ-Fe_2O_3 is ferromagnetic. Fe_3O_4 can easily oxidize to γ-Fe_2O_3. Therefore, in our case we have to consider the magnetization of Fe as metal or as γ-Fe_2O_3. The magnetization of Fe and γ-Fe_2O_3 for 0.088 ppm is of 10^{-3} order. Similarly, metallic Co and Ni are ferromagnetic, whereas Co_3O_4 and NiO are antiferromagnetic. The maximum contribution from both the phases of Co is of the order of 10^{-4} emu/g and from Ni is 10^{-3} emu/g. In our case we have got magnetization of SnO_2 of the order of 10^{-1} emu/g. Therefore, we conclude that the magnetization values reported in this work are not due to impurities and it is intrinsic in SnO_2. Fig. 7(a) shows room temperature (300 K) hysteresis loops of $TO_{Vac}200$ and TO200. Even though both samples show RT ferromagnetism, the saturation magnetization (M_s) appears to be higher in TO200 than in $TO_{Vac}200$. The values of M_s and H_c (coercivity) and M_r (remanence) of both the samples are inserted in Table 1. M_s & H_c for TO200 are found to be 0.16 emu/g and 63 Oe respectively. As table I shows, H_c decreases with increase in M_s, which is also consistent with the equation[32] $H_c = 2K_1/M_s$, where K_1 is the anisotropy constant. Arrot-Belov-Kouvel (ABK)[28] plot of $TO_{Vac}200$ and TO200 is demonstrated in Fig. 7(b). In the ABK plot, M^2 is plotted against H/M and the spontaneous magnetization is measured from the intercept of the linear fitting of the curve on Y-axis. ABK plot signifies the presence of ferromagnetic interaction and measures the spontaneous magnetization in the sample. The spontaneous magnetizations of TO200 and $TO_{Vac}200$ are 0.03 and 0.02 emu/g respectively. The increase in spontaneous magnetization of TO200 indicates the presence of long range ferromagnetic ordering.

For a better understanding of the magnetic property in the system we have also carried out zero field cooling (ZFC) and field cooling (FC) measurements of TO200 in the temperature range of 4 to 350 K at an applied field of 100 Oe, as shown in Fig. 8. The bifurcation between FC and ZFC up to 350 K indicates the presence of ferromagnetic interaction in the system. Several factors might affect this bifurcation including magnetic anisotropy in the system, coercive field and the way by which FC and ZFC measurements are being carried out. Absence of characteristic sharp peak or hump in the ZFC curve

signifies that the observed ferromagnetism is intrinsic in nature and there is no blocking of spins. Both M-H and M-T measurements indicate presence of room temperature ferromagnetism in the system. The high value of M_s of TO200 as compared to vacuum annealed sample indicate that vacuum annealing do affect the magnetic property. It is known that annealing of SnO_2 nanoparticles under vacuum removes the loosely bound oxygen atoms on the surface and generates oxygen vacancies. The paramagnetic oxygen species that may contribute towards magnetism are (i) oxygen vacancies with single trapped electron[8] (F^+) and (ii) single electron trapped oxygen molecules (O_2^-). Although we have not found direct confirmation of the presence of F^+ center from EPR, presence of O^{2-} signal might indicate that F^+ centers are present on the surface. The single trapped electron might be easily transformed to adsorbed O_2 molecule and forms O_2^- species. We could believe that vacuum annealing has increased the density of oxygen vacancies and thus, the density of paramagnetic superoxide species. Because of the presence of higher numbers of electron spins in $TO_{Vac}200$ one could expect high magnetization in $TO_{Vac}200$ as compared to TO200. Instead, the lowering of both saturation and spontaneous magnetization in $TO_{Vac}200$ might indicate that the oxygen vacancies (or to mention superoxide species) have negative impact on the total magnetization.

Therefore, it is likely that cationic Sn^{4+} vacancy might be affecting the ferromagnetism. Earlier reports summarized that cationic vacancies could produce magnetism in different oxide systems.[12-14,33,34] Initially prepared SnO_2 nanocrystallites may contain considerable numbers of Sn^{4+} and oxygen vacancies on the surface. On air annealing of as prepared SnO_2 powder at 200 ^{0}C, most of the oxygen vacancies disappeared and thus, only Sn^{4+} vacancies are left. These Sn^{4+} vacancies should contribute to magnetism but there is ambiguity in the literature reports on the observed magnetism in SnO_2.[7,9, 35] Our experimental results indicate that oxygen and Sn^{4+} vacancies have respectively negative and positive contribution to the observed magnetism. In order to establish the roles of oxygen and Sn^{4+} vacancies in ferromagnetism, we also performed theoretical calculations based on DFT. We have thus calculated electronic properties of several point defects starting from vacancies to interstitial in two different model structures of SnO_2 {Surface (110) and Supercell}.

4.3. Electronic structure and magnetic calculation

We have computed both surface and supercell structures and did a detail DFT based investigation on different kind of vacancies to arrive at a model which explains the observed magnetism in pristine SnO_2 nanosystem annealed in vacuum and air. We have considered SnO_2 (110) surface having 48 atoms and relaxed the structure to settle for minimum energy configuration. As we know the surface to volume ratio in nano regime is very high. The contribution from surface part is very prominent and its effect on magnetism has to be considered. We have chosen the surface calculation because most of the Sn atoms and oxygen atoms are not adequately compensated with bonds. The magnetism arises in the system due to 2p state of O (a). Both these oxygen are single bonded and are not compensated. Fig. 9 shows the total density of states (TDOS) plot for SnO_2 where the partial density of states (PDOS) of O (a) split up near the Fermi level (0 eV). The TDOS of SnO_2 (110) shows the hybridization of Sn 5*s* and Sn 5*p* states with O 2*p* states at the top of the valence band where Sn 5*s* state is dominant over Sn 5*p*, which indicates the formation of free holes.[36] The asymmetric distribution of spin density around the Fermi level indicates the presence of magnetism in the system. If we put any further Sn^{4+} vacancy or oxygen vacancy or a Sn interstitial, the magnetism appears to be decreased. This shows that the resultant magnetic moment of 1.2 μ_B is due to the reduction of SnO_2 from bulk to surface and any further impurity does not increase the magnetic moment. The PDOS of oxygen proves the fact that these are the spin polarized oxygen which induces magnetism in pure layer of SnO_2.

We have also investigated the supercell of SnO_2 containing a total of 48 atoms. We studied the effect of intrinsic defects on the structure and the magnetism. Pure SnO_2 supercell $Sn_{16}O_{32}$ has no magnetism at all and this is quite expected as there are no dangling bonds of Sn or oxygen. We initially introduced oxygen vacancies, next Sn vacancies and then Sn interstitial. The defect formation energy $E_f(D)$ is calculated using

$$E_f(D) = E_d - E_p + \tfrac{1}{2} n_O E(O_2) + n_{Sn} E(Sn) + n_O \mu_O + n_{Sn} \mu_{Sn} \quad \text{.....(iv)}$$

Where E_d, E_p, E (O_2) and E (Sn) are the total energy of the supercell with defect, pure supercell, oxygen molecule and single Sn atom. n_O and n_{Sn} are the number of O and Sn vacancy, while μ_O and μ_{Sn} are the chemical potential of O and Sn respectively. The values of μ_O and μ_{Sn} are external environment dependent i.e., it depends on the oxygen partial pressure. The two extreme conditions are known as O poor and O rich condition.[17] The value of formation energy of $Sn_{15}O_{32}$ (single Sn vacancy), $Sn_{16}O_{31}$ (single O vacancy) and $Sn_{17}O_{32}$ (single Sn interstitial) are given in table II. We have seen that forming an oxygen vacancy under O poor condition and forming a Sn vacancy under O rich condition is energetically favorable. The formation of Sn interstitial neither in O rich nor O poor condition seems to be energetically favorable. This implies that formation of oxygen vacancy in $TO_{Vac}200$ and the formation of Sn vacancy in TO200 are easier to achieve. The formation energy values shown in table II cannot be directly compared to the required experimental formation energy values in $TO_{Vac}200$ and TO200, but still the pattern of formation of defects can be understood. The magnetic moment values determined based DFT based results are listed in table II. We checked it for different positions for oxygen vacancies but it did not result any magnetism. From table II it is clear that in an ordered SnO_2, we get maximum value of magnetization when Sn^{4+} vacancies are introduced. From our calculation we have found that the major contribution in $Sn_{15}O_{32}$ comes from the surrounding oxygen named as O (a-f), as shown in magnetization density mapping of Fig. 10. Further O (a) has same contribution as that of O (c), similarly O (b) is same as O (d) and O (e) is same as O (f). We have checked the splitting of oxygen near the Fermi level by plotting PDOS of oxygen as shown in Fig. 11. The asymmetric distribution of spin up and spin down states for oxygen (a-f) near and above the Fermi level confirms the magnetic nature of the system. We have also calculated the formation energy of oxygen and Sn vacancy on the surface (110) plane of SnO_2 and inserted the values in table II. We have found that the formation energy of oxygen vacancy in O deficient condition is very low, while its formation in O rich condition is relatively harder (with high formation energy). The formation energy of Sn vacancy in O deficient condition is very high, while the corresponding value is very low in O rich condition. In the bulk calculation the formation energy of

oxygen vacancy and Sn vacancy in two different conditions are found to be of same pattern though values are higher in this case compared to surface (110). Our claim that Sn vacancies are the source of magnetism can be verified by the result of formation of Sn vacancies in SnO_2. Both in bulk and surface Sn vacancies formation are easier to achieve in O rich condition that in O deficient condition. On the other hand oxygen vacancies instantaneously forms under O deficient condition in SnO_2 (110) surface and at slightly high energy cost in bulk SnO_2.

4.4. Correlation between DFT and experimental results

From the experimental and theoretical investigations it seems that the origin of magnetism in SnO_2 is not due to oxygen vacancies but because of Sn vacancy or the magnetism is hole mediated. From DFT calculation it is observed that the valence band splitting and spin polarization is observed near the Fermi level in $Sn_{15}O_{32}$. This splitting is due to the formation of four holes (Sn^{4+} vacancy). The holes are distributed on the lattice oxygen nearest to Sn vacancy and the surrounded oxygen is spin polarized. However, in $TO_{Vac}200$ the number of lattice oxygen surrounding Sn vacancy will be diminished. Therefore, loss of polarized oxygen around Sn vacancy will lead to reduction in average magnetization in $TO_{Vac}200$.[37] Although our EPR results indicated that the relative numbers of unpaired spins on the oxygen vacancies are higher in $TO_{Vac}200$, these unpaired spins have no positive influence on the total magnetization. Zhang *et al.* reported that point defects with local moments may not necessarily contribute towards ferromagnetism.[38] In the present study anionic point defects (oxygen vacancies) have no role in ferromagnetism, whereas cationic defects (Sn vacancy) has certainly the major contribution to ferromagnetism. From our results we have found that formation of Sn vacancy is favorable in TO200 and formation of oxygen vacancy is favorable in $TO_{Vac}200$. Sn vacancy polarizes the nearest lattice oxygen and induces magnetic moment in them, whereas presence of oxygen vacancies reduces the number of polarized oxygen and reduces the magnetic moment. Apart from Sn^{4+} vacancies, the smaller size of TO200 than $TO_{Vac}200$ might be another possible reason of superior magnetization of TO200 over

$TO_{Vac}200$. The first effect (magnetization due to Sn^{4+} vacancy) is described by the supercell approach while the second effect (reduction in size) is understood by considering surface (110) calculation. In the present study the adsorbed O_2 molecule has negative impact on the magnetization. The numbers of these adsorbed O_2 molecule are expected to be very high on the surface of $TO_{Vac}200$ than in TO200. We believe that because of the presence of high density of oxygen vacancy sites on the surface of $TO_{Vac}200$, the O_2 molecule can be easily adsorbed on the surface oxygen vacancies. However, in TO200 the numbers of surface oxygen vacancies are comparatively less and thus, the adsorption sites for O_2 are expected to be very few. Unlike TO200 where hole trapped in lattice oxygen atom, surrounding Sn vacancy, becomes advantageous for high magnetization, the additional surface adsorbed O_2 molecule with trapped electron (or O_2^-) in $TO_{Vac}200$ has no contribution to the total magnetization.

5. Conclusion

A detailed study on structural and magnetic property is done on the SnO_2 nanosystems annealed in vacuum and air at 200 ^{0}C. XRD and Raman study reveals that $TO_{Vac}200$ have both SnO and SnO_2 phase in the system. Room temperature ferromagnetism is because of the presence of Sn vacancy. Formation of Sn vacancy releases hole which are trapped on the nearest lattice oxygen, and on application of magnetic field the spins in 2*p* orbital of oxygen are polarized with induced magnetic moment. Vacuum annealing will result in the removal of polarized lattice oxygen surrounding Sn vacancy and thus, a reduced magnetic moment is resulted. DFT spin polarized structural optimization on SnO_2 (110) and SnO_2 supercell supports the experimental results and predicts that magnetism in this system might arise due to the presence of Sn^{4+} vacancies. Oxygen vacancies have no contribution to ferromagnetism in SnO_2. Defect formation energy values shows that formation of Sn vacancies in O rich system is energetically favorable compared to other point defects. The DFT prediction seems to justify the observed higher saturation magnetization of TO200 as compared to oxygen deficient $TO_{Vac}200$.

Acknowledgement: Pawan Chetri likes to acknowledge DST for providing Inspire fellowship. Biswajit Choudhury and Amarjyoti Choudhury acknowledge the financial support provided by Department of Science and Technology (DST), India, to the project SR/NM/NS-98/2010 (G). We want to thank SAIF IIT Bombay for helping us in carrying out the EPR measurement and IIT Kharagpur for carrying out SQUID measurement.

References

[1] D. D. Awschalom, L. C. Bassett, A. S. Dzurak, E. L. Hu and J. R. Petta, *Science*, 2013, **339**, 1174.

[2] T. Sabergharesou, T. Wang, L. Ju and P. V. Radovanovic, *Appl. Phys. Lett.*, 2013, **103**, 012401.

[3] J. M. D. Coey, A. P. Douvalis, C. B. Fitzgerald and M. Venkatesan, *Appl. Phys. Lett.*,2004, **84**, 1332.

[4] Y. Li, R. Deng, Y. Tian, B. Yao and T. Wu, *Appl. Phys. Lett.* , 2012, **100**, 172402.

[5] B. Y. Zhang, B. Yao, Y. F. Li, A. M. Liu, Z. Z. Zhang, B. H. Li, G. Z. Xing, T. Wu, X. B. Qin, D. X. Zhao, C. X. Shan and D. Z. Shen, *Appl. Phys. Lett.*, 2011, **99,** 182503.

[6] S. B. Ogale, R. J. Choudhary, J. P. Buban, S. E. Lofland, S. R. Shinde, S. N. Kale, V. N. Kulkarni, J. Higgins, C. Lanci, J. R. Simpson, N. D. Browning, S. D. Sarma, H. D. Drew, R. L. Greene and T. Venkatesan, *Phys. Rev. Lett.*, 2003, **91**, 077205.

[7]A. Sundaresan, R. Bhargavi, N. Rangarajan, U. Siddesh and C. N. R. Rao, *Phys. Rev. B*, 2006, **74**, 161306.

[8] V. B. Kamble, S. V. Bhat and A. M. Umarji, *J. Appl. Phys.*, 2013, **113**, 244307.

[9] N. H. Hong, N. Poirot and J. Sakai, *Phys. Rev. B*, 2008, **77**, 033205.

[10] L. Zhang, S. Ge, Y. Zuo, B. Zhang and L. Xi, *J. Phys. Chem. C*, 2010, **114**, 7541.

[11] K. C. Zhang, Y. Liu, Y. F. Li and Y. Zhu, *J. Appl. Phys.*, 2013, **113**, 053713.

[12] A. Espinosa, N. Sanchez, J. Sanchez-Marcos, A. D. Andres and M. C. Munoz, *J. Phys. Chem. C*, 2011, **115**, 24054.

[13] A. Rusydi et.al, *Philos. Trans. R. Soc. A*, 2012, **370**, 4927.

[14] D. C. Qi, *Phy. Rev. B*, 2013, **87**, 245201.

[15] S. Ghosh, M. Mandal and K. Mandal, *J. Magn. Magn. Mater*, 2011, **323**, 1083.

[16] P. Chetri and A. Choudhury, *Physica E*, 2013, **47**, 257.

[17] K. G. Godinho, A. Walsh and G. W. Watson, *J. Phys. Chem. C*,2009, **113**, 439.

[18] R. S. Katiyar, *J. Phys. C*, 1970, **3**, 1087.

[19]J. G. Traylor, H. G. Smith, R. M. Nicklow and M. K. Wilkinson, *Phys.Rev. B*, 1971, **3**, 3457.

[20] P.Chetri, B. Saikia and A. Choudhury, *J. Appl. Phys.*, 2013, **113**, 233514.

[21] C.H. Shek, G.M. Lin and J.K.L. Lai, *Nanostruct. Mater.*, 1999, **11**, 831.

[22] J. Geurts, S. Rau, W. Richter and F.J. Schmitte, *Thin Solid Films*, 1984, **121**, 217.

[23] V. G. Kravets, *Optics and Spectroscopy*, 2007, **103**, 766.

[24] D. Zwingel, *Phys. Stat. Sol. (b)*, 1976, **77**, 171.

[25] G. Yang, Z. Jiang, H. Shi, T. Xiao and Z. Yan, J. Mater. Chem., 2010, **20**, 5301.

[26]A. Gurlo, *Chem Phys Chem.*, 2006, 7, 2041.

[27] B. M. Maoz, E. Tirosh, M. B. Sadan and G. Markovich, *Phys. Rev. B*, 2011, **83**,161201.

[28] B. Choudhury and A.Choudhury, *J.Appl.Phys.*, 2013, **114**, 203906.

[29] S.K. Song, J.S. Cho, W.K. Choi, H.J. Jung, D. Choi, J.Y. Lee, H.K. Baik and S. K. Koh, *Sensor Actuat B-Chem*,1998, **46**, 42.

[30] I.S. Mulla, V.J. Rao, H.S. Soni, S. Badrinarayanan and A.P.B. Sinha, *Surf. Coat. Tech.*,1987, **31**, 77.

[31]P. K. Biswas, A. De, L. K. Dua and L. Chkoda, *Bull. Mater. Sci.*, 2006, **29**, 323.

[32] P. S. A. Kumar, P. A. Joy and S. K. Date, *Bull.Mater.Sci.*, 2000, **23**, 97.

[33] H. Ren, G. Xiang, G. Gu, X. Zhang, W. Wang, P. Zhang, B. Wang and X. Cao, *J.Nano Mat.*, 2012, **2012**, 295358.

[34] S. Ghosh, G. G. Khan, B. Das and K. Mandal, *J. Appl. Phys.*, 2011,**109**,123927.

[35] G. Rahman, V. M. Garcia-Suarez and S. C. Hong, *Phys. Rev. B,* 2008, **78**, 184404.

[36] P. Barquinha, R. Martins, L. Pereira and E. Fortunato, Transparent Oxide Electronics from Materials to Devices, Willey, West Sussex , 2012

[37] A. Espinosa, N. Sanchez, J.S. Marcos, A. Andres and M.C. Munoz, *J. Phys. Chem. C*, 2011, **115**, 24054.

[38] C. W. Zheng, H. Kao and J.M. Dong, *Phys. Lett. A.*, 2009, **373**, 2592.

Figure captions:

Fig.1 XRD pattern of TO200 and $TO_{Vac}200$.

Fig.2 High resolution TEM images of $TO_{Vac}200$ (a & b) and TO200 (c & d) respectively. Histogram in the inset of Fig. 2a and Fig. 2c shows size distribution of the nanoparticles.

Fig. 3 Room temperature Raman Spectra of $TO_{Vac}200$ and TO200. The position of A_{1g} peak is shifted towards higher energy side in $TO_{Vac}200$.

Fig.4 Room temperature electron paramagnetic resonance (EPR) spectra of $TO_{Vac}200$ and TO200.

Fig.5 X-ray photoelectron spectra (XPS) of $TO_{Vac}200$.

Fig.6 X-ray photoelectron spectra (XPS) of TO200.

Fig.7 (a) Room temperature M-H curves of TO200 and $TO_{Vac}200$. (b) Arrot-Belov-Kouvel (ABK) plot for the determination of spontaneous magnetization in TO200 and $TO_{Vac}200$ respectively.

Fig.8 Zero field cooling (ZFC) and field cooling (FC) temperature dependent magnetization (M-T) curves of TO200. Inset of the figure shows the extended part of the curve in the temperature range of 200-350 K to display the complete separation of ZFC and FC upto 350 K.

Fig.9 Total density of states (TDOS) plot of SnO_2 (110) and PDOS plot of O (a), Sn 5s and Sn 5p. Red lines indicate *p* state while black line indicated *s* state. The Fermi level is shown by blue line (at 0 eV).

Fig. 10 (a) Magnetization density develops in SnO_2 surface (110). (b) 2x2x2 supercell of SnO_2 (right) and magnetization density develops in the system due to Sn vacancy. Yellow atom denotes Sn, red denotes Oxygen and white denotes Sn vacancy.

Fig.11 TDOS plot of $Sn_{15}O_{32}$ supercell (with one Sn vacancy) and PDOS of O (a, b, e). Red lines indicate *p* state while black line indicated s state whereas Fermi level is shown by blue line (at 0 eV).

FIGURE FILES

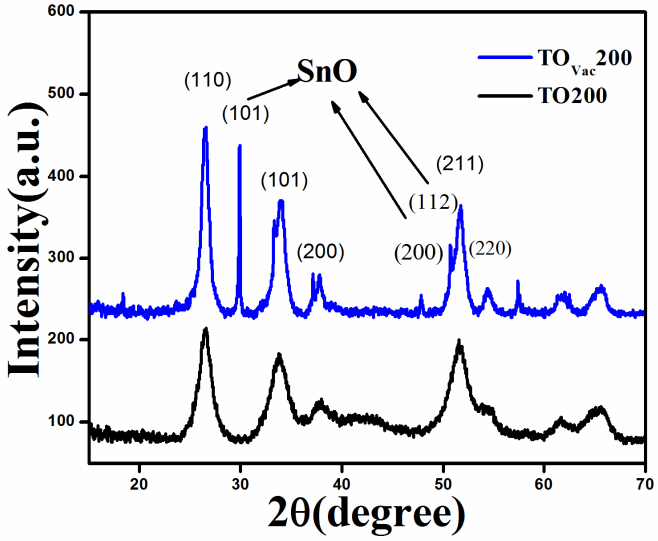

Figure 1

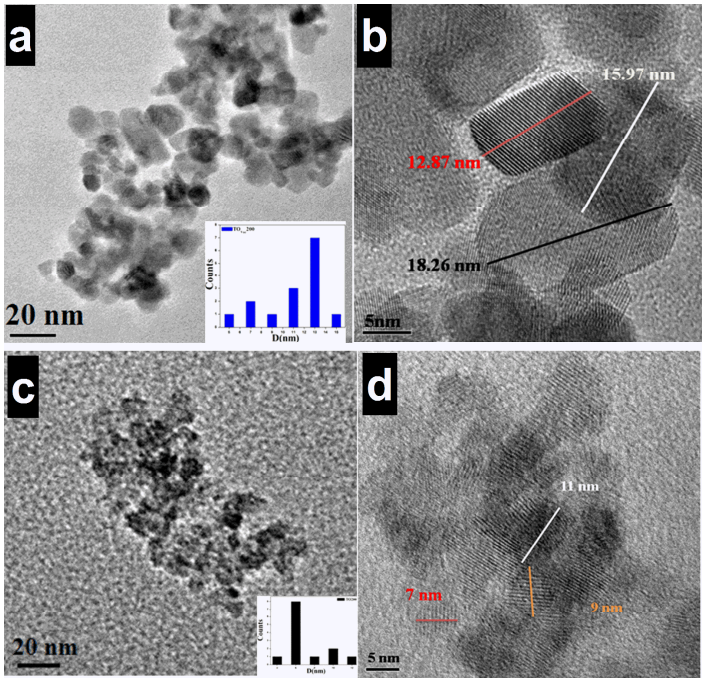

Figure 2

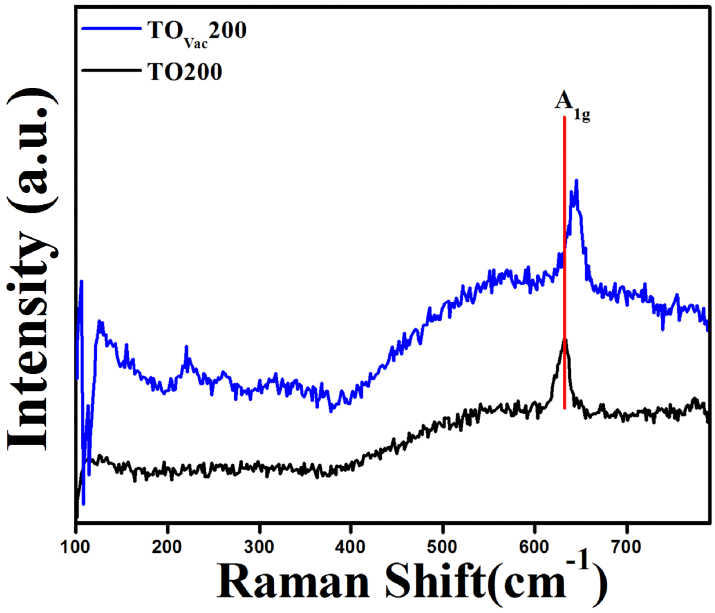

Figure 3

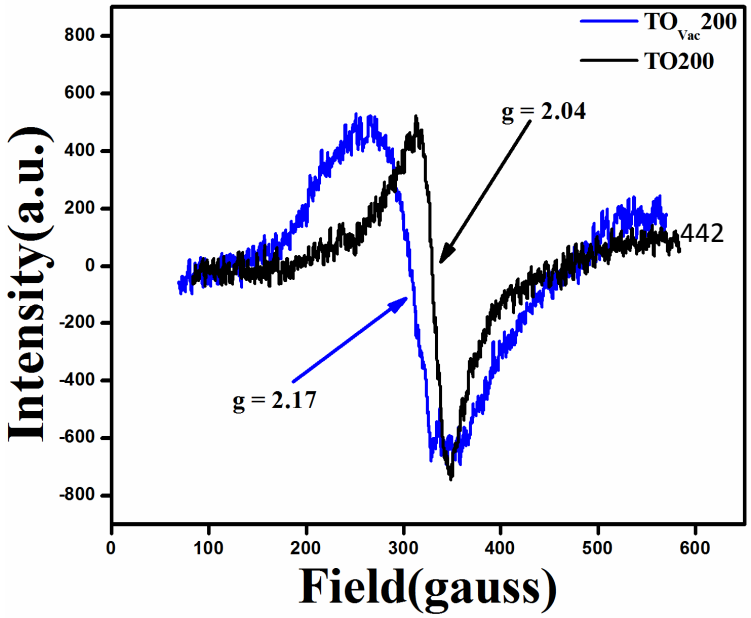

Figure 4

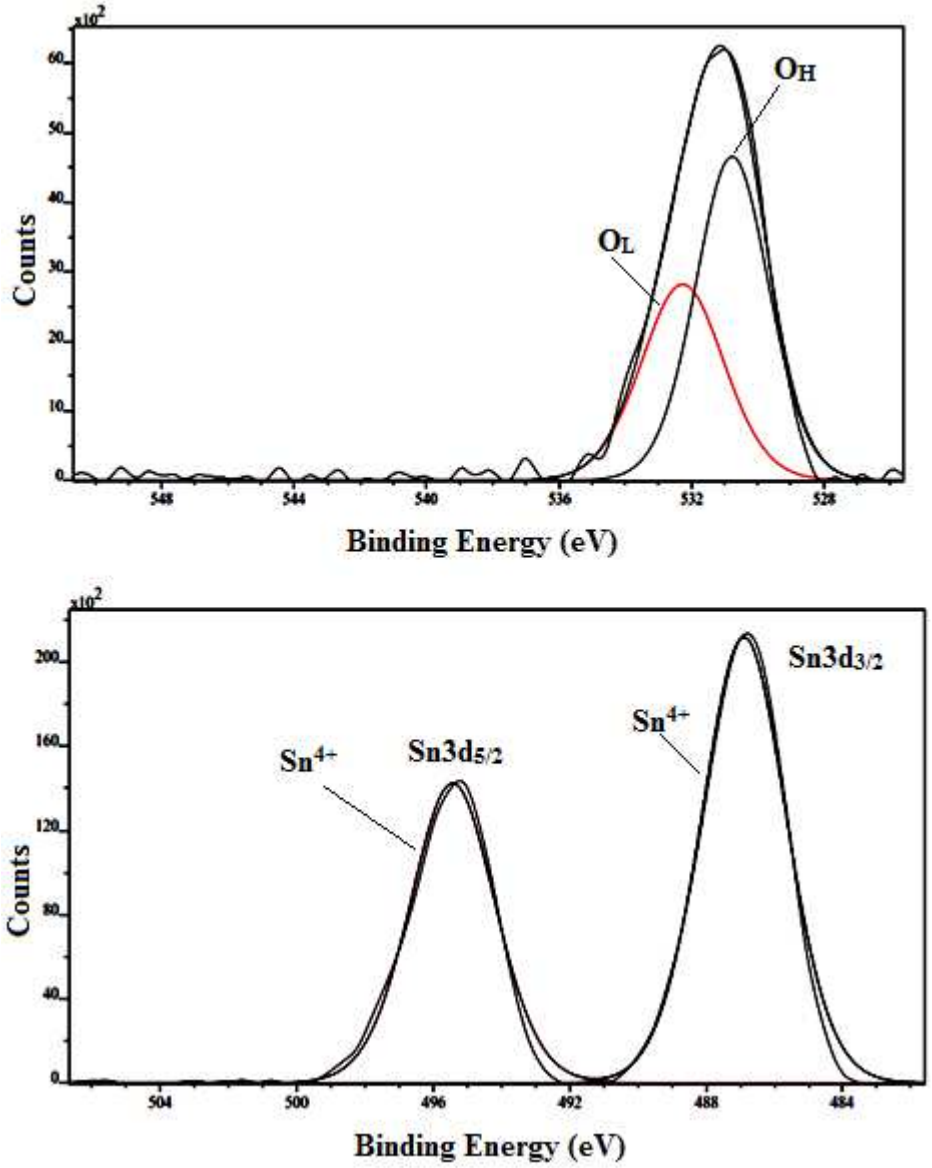

448

449

450 **Figure 5**

451

452

453

454

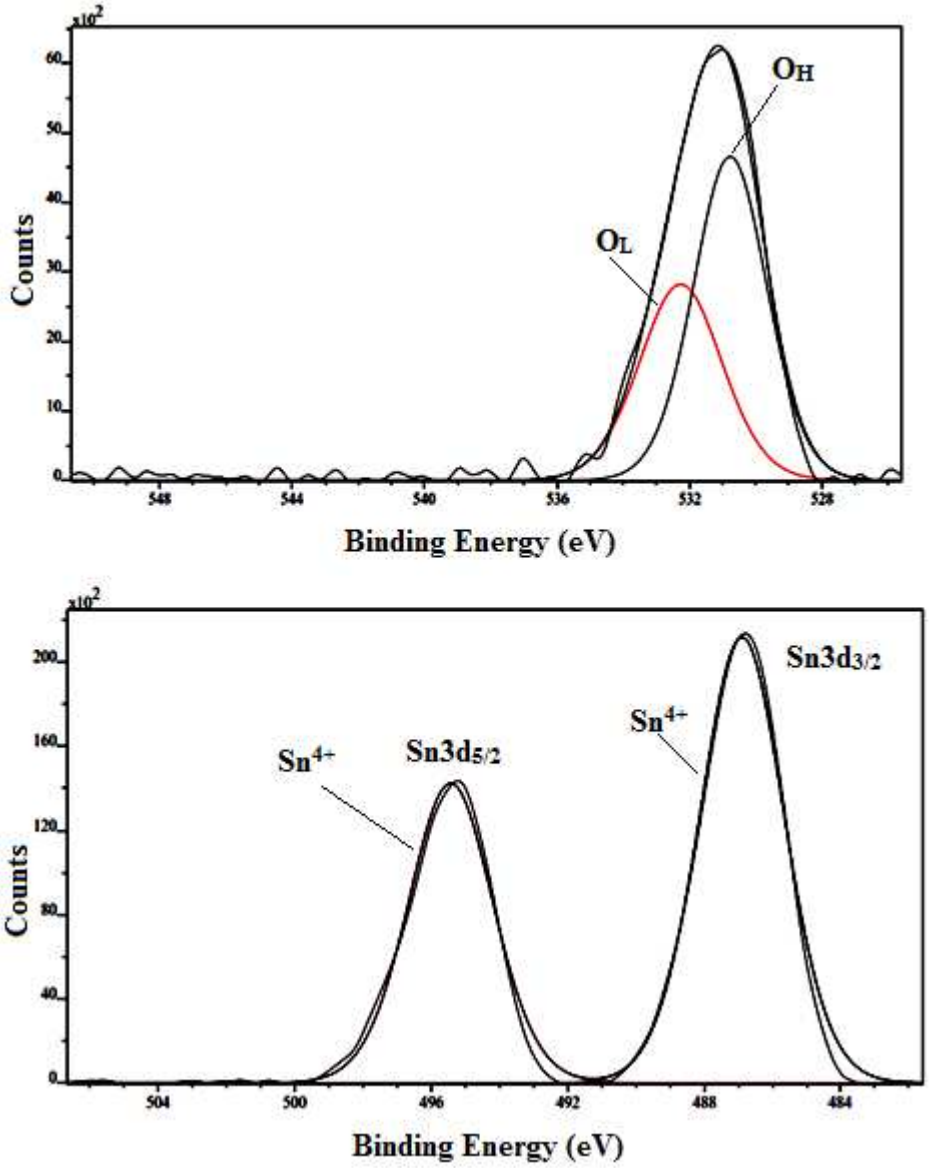

Figure 6

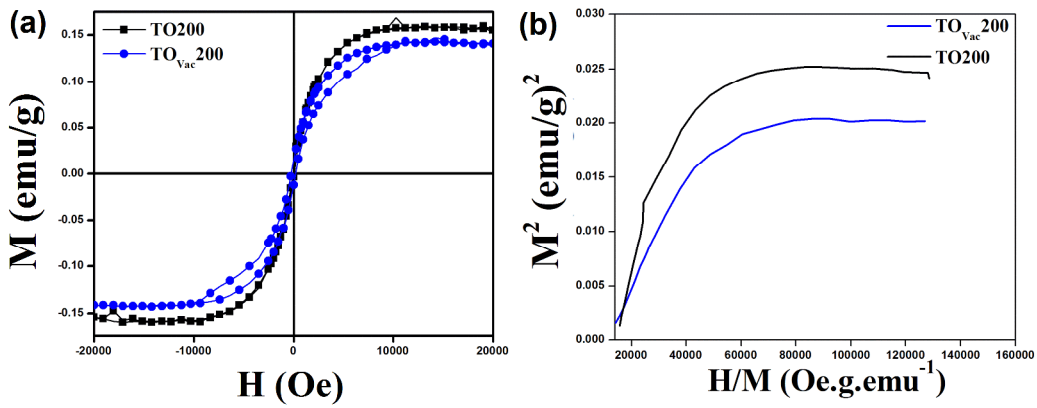

Figure 7

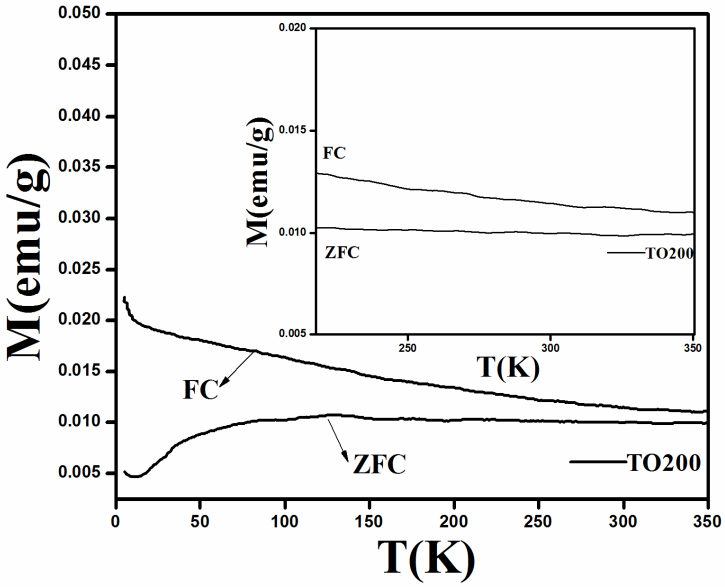

Figure 8

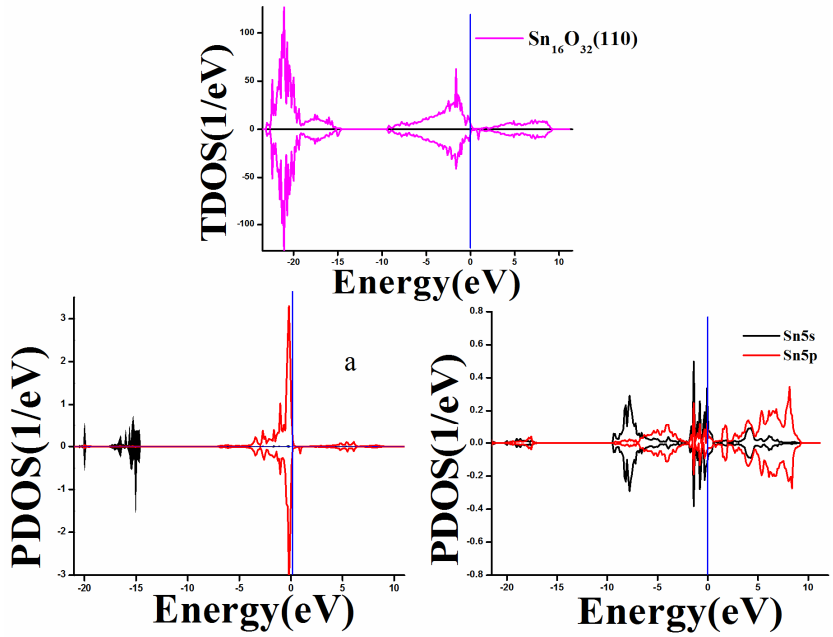

Figure 9

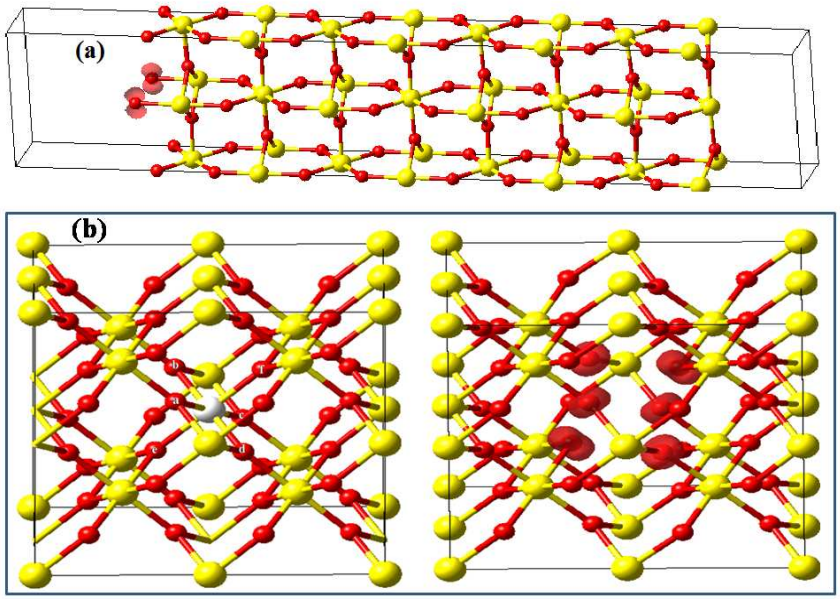

Figure 10

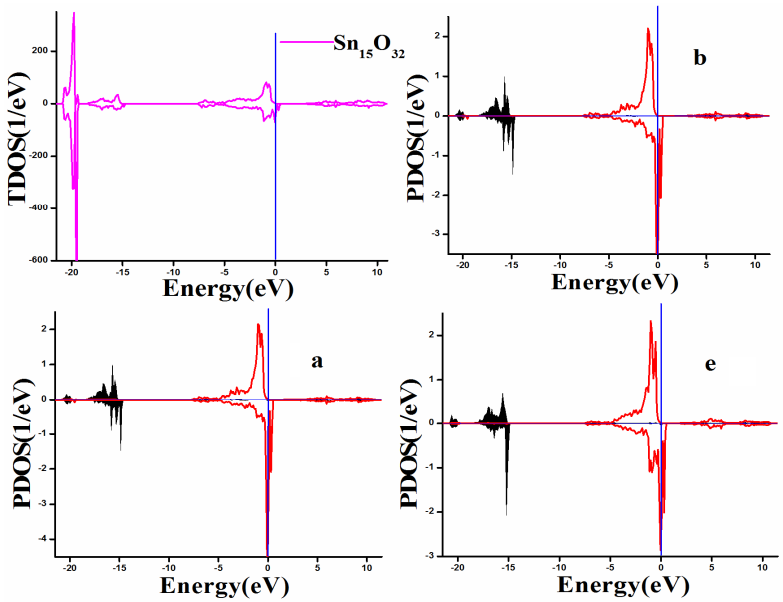

Figure 11

Table I Crystallite size, saturation magnetization (M_s), coercivity (H_c) and remanence (M_r) of TO200 and $TO_{Vac}200$

System	Crystallite Size (nm) from Scherer formula	M_s (emu/g)	H_c (Oe)	M_r (emu/g)
TO200	5.44	0.16	63	0.005
$TO_{Vac}200$	12.50	0.14	200	0.011

Table II: Different systems, defect formation energy (eV) in O excess and O poor condition and total Magnetic moment

System	Defect formation energy E_f (D)(eV)		Total magnetic moment (μ_B)
	O excess condition	O poor condition	
$Sn_{16}O_{32}$	--	--	0.0
$Sn_{15}O_{32}$	1.3	7.5	3.9
$Sn_{16}O_{31}$	3.5	0.4	0.0
$Sn_{17}O_{32}$	14.3	8.2	0.0
SnO_2(110)	--	--	1.2
SnO_2(110) with Sn vacancy	0.9	7.1	
SnO_2(110) with O vacancy	1.6	-1.4	